ACS OMEGA

http://pubs.acs.org/journal/acsodf

Article

Mesoporous Octahedron-Shaped Tricobalt Tetroxide Nanoparticles for Photocatalytic Degradation of Toxic Dyes

Vaishali N. Sonkusare, Ratiram Gomaji Chaudhary,* Ganesh S. Bhusari, Aniruddha Mondal,* Ajay K. Potbhare, Raghvendra Kumar Mishra, Harjeet D. Juneja, and Ahmed A. Abdala*

Cite This: *ACS Omega* 2020, 5, 7823−7835

Read Online

ACCESS | Metrics & More | Article Recommendations | Supporting Information

ABSTRACT: The present article reports a facile approach to fabrication of mesoporous octahedron-shaped tricobalt tetroxide nanoparticles (Co_3O_4 NPs) with a very narrow size distribution for eco-friendly remediation of toxic dyes. Co_3O_4 NPs were fabricated by a sol−gel process using cobalt chloride hexahydrate ($CoCl_2 \cdot 6H_2O$) and monosodium succinate ($C_4H_5O_4Na$) as a chelating/structure-directing agent and sodium dodecyl sulfate as a surfactant. Moreover, the phase structure, elemental composition, and thermal and morphological facets of Co_3O_4 NPs were investigated using XRD, FT-IR, EDS, Raman, XPS, TGA, SEM, and TEM techniques. The face-centered cubic spinel crystalline structure of the Co_3O_4 NPs was confirmed by XRD and SEM, and TEM analysis revealed their octahedron morphology with a smooth surface. Moreover, the narrow pore size distribution and the mesoporous nature of the Co_3O_4 NPs were confirmed by Brunauer−Emmett−Teller measurements. The photocatalytic activity of Co_3O_4 NPs for degradation of methyl red (MR), Eriochrome Black-T (EBT), bromophenol blue (BPB), and malachite green (MG) was examined under visible light irradiation, and the kinetics of the dye degradation was pseudo-zero-order with the rate constant in the order of MR > EBT > MG > BPB. Furthermore, the mechanism of photo-disintegration mechanism of the dye was examined by a scavenging test using liquid chromatography−mass chromatography, and its excellent photodegradation activities were attributed to the photogenerated holes (h^+), superoxide (O_2^-) anions, and hydroxyl ($^{\cdot}OH$) radicals. Finally, the synergistic effect of the nano-interconnected channels with octahedron geometry, mesoporous nature, and charge transfer properties along with photogenerated charge separations leads to an enhanced Co_3O_4 photocatalytic activity.

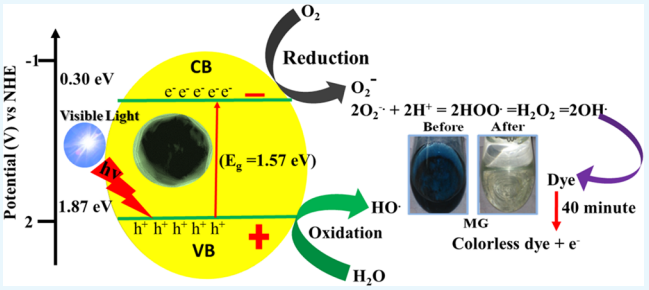

INTRODUCTION

Today's major concern is to get clean water owing to fast civilization and industrialization, which is an essential for the survival of living organisms. In recent years, the extensive use of carcinogenic organic dyes in the textile industry has increased gradually and increased amounts of pollutant effluents have been released into aquatic ecosystems.[1−6] This causes depletion of the dissolved oxygen content, which has adverse effects on aquatic creatures and mankind.[7−9] Toxic dyes such as methyl red (MR), Eriochrome Black-T (EBT), bromophenol blue (BPB), and malachite green (MG) are significantly used in textiles, paper making, and pharmaceuticals[10−12] due to their relatively low cost even though they are known to have harmful effects on the reproductive system, genotoxicity, and carcinogenic properties.[13−15] These dyes are difficult to eradicate by conventional techniques such as adsorption, coagulation, flocculation, biodegradation, and so forth.[7,9,10,16] All these methods are expensive and require extra planning to remove the byproducts. Alternatively, photocatalytic degradation of toxic dyes into nontoxic compounds is the most desirable process to mitigate their environmental impact.[17,18] Thus, it is indispensable to develop a possible permanent solution for the degradation of toxic dyes in wastewater streams.

Transition-metal oxide-catalyzed photocatalytic degradation has emerged to be a low-cost, environmentally friendly, and efficient method for dye-based effluent treatments compared to its abovementioned counterparts.[19−23] Due to their mixed oxidation states, transition-metal oxides have gained remarkable consideration in cutting-edge days, and due to their unique physicochemical and electromagnetic properties, they show potential applications in diverse areas such as wastewater treatment, lightweight fillers, catalysis, supercapacitors, gas sensors, lithium-ion batteries, and chemical storage.[24−27] Among the transition-metal oxides, spinel-tricobalt tetroxide

Received: November 24, 2019
Accepted: March 19, 2020
Published: April 1, 2020

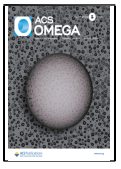

https://dx.doi.org/10.1021/acsomega.9b03998
ACS Omega 2020, 5, 7823−7835

Scheme 1. Synthesis of Octahedron-Shaped Co_3O_4 NPs

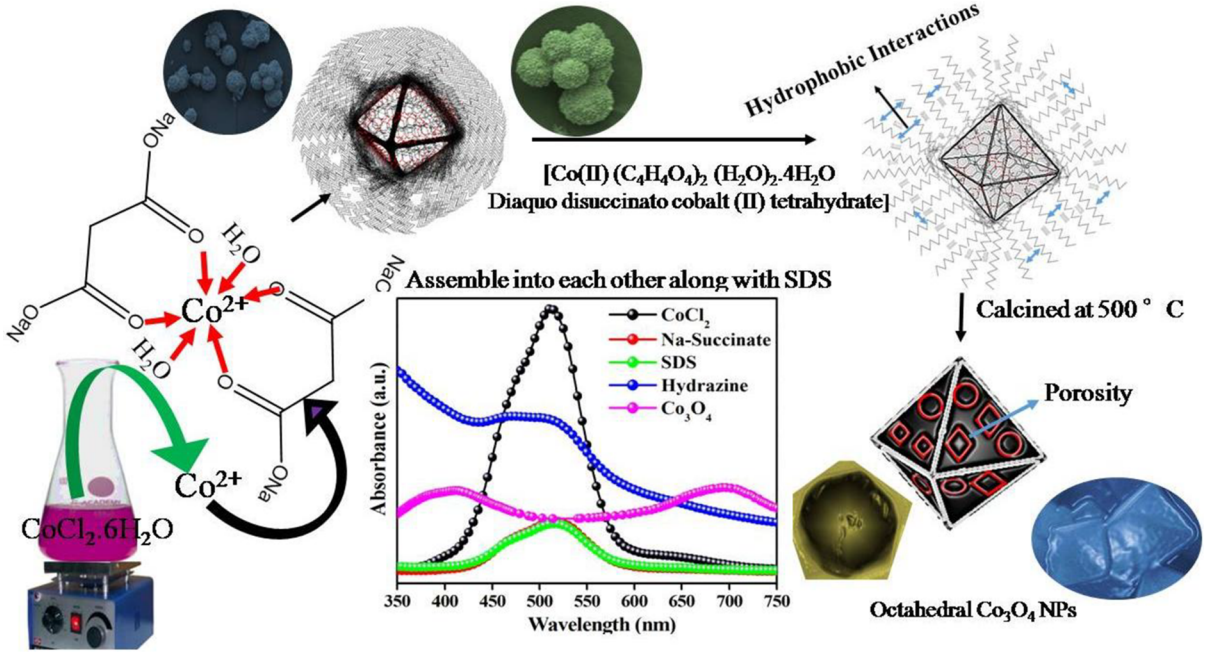

(Co_3O_4) occasionally symbolized as $CoO{\cdot}Co_2O_3$ and analogous to $FeO{\cdot}Fe_2O_3$ has emerged rapidly as one of the most popular spinel materials due to its unique properties, chemical stability, and facile synthesis method.[25,28,29] Furthermore, Co_3O_4 belongs to three types of cobalt oxide families, and the other two oxides are rock salt (CoO) and hexagonal Co_2O_3.[30] It is well known that Co_3O_4 is a p-type semiconducting material, and in its spinel structure, Co^{2+} ions occupy the tetragonal 8(a) sites, Co^{3+} ions occupy the octahedral 16(d) sites, and O^{2-} ions are located at 32(e) sites arranged in a cubic close-packed structure.[24,31]

Previously, diverse approaches have been adopted for the preparation of spinel-Co_3O_4 nanoparticles (NPs) such as chemical vapor deposition at 550 °C, thermal decomposition of cobalt precursors under oxidizing conditions around 210−815 °C, chemical spray pyrolysis at 350−400 °C, pulsed laser deposition (PLD), and electron beam deposition.[32−35] However, these routes require severe conditions, relatively high temperatures, and some special instruments. Furthermore, the application of these conventional approaches for the synthesis of Co_3O_4 NPs is limited by their low productivity. Moreover, a number of research groups have reported the preparation of mesoporous Co_3O_4 NPs by electrospinning and calcination of mixed polymeric templates such as poly(vinylpyrrolidone) (PVP) and poly(ethylene glycol) (PEG) for visible light photocatalytic applications.[6] It is revealed that the use of low- and high-molecular-weight polymers (PVP and PEG), hydrogen bonding between the polymer and metal hydroxide, and hydrophilicity of PEG are responsible for the formation of a mesoporous structure, which provides more surfaces for photocatalytic degradation.[5,6]

We have recently developed facile routes for the synthesis of monodisperse CuO, spinel-$CuAl_2O_4$, and novel γ-Bi_2O_3 microspindles for antioxidant, electrochemical, and photocatalytic applications.[36−38] In the present study, we have developed a simple protocol for large-scale fabrication of octahedron-shaped Co_3O_4 NPs by a sol−gel method using monosodium succinate ($C_4H_5O_4Na$) and sodium dodecyl sulfate ($NaC_{12}H_{25}SO_4$) at a low temperature (50 °C) followed by calcination at 500 °C for 3 h. The as-fabricated Co_3O_4 NPs in the presence and absence of SDS were characterized by an array of analytical techniques for their structural, compositional, and morphological characteristics.

There are a number of reports on the photodegradation of methylene blue,[33] Rhodamine B, and Direct Red 80[35] using Co_3O_4. Therefore, we here focused on low-temperature fabrication of mesoporous spinel-Co_3O_4 NPs using a sol−gel method and their application for the photocatalytic degradation of toxic organic dyes [methyl red (MR), Eriochrome Black-T (EBT), bromophenol blue (BPB), and malachite green (MG)].

Moreover, detention of the trapping species assay was carried out using potassium iodide (KI), potassium bromate (KB), sodium thiosulfate (ST), and benzoquinone (BQ) as scavengers, and a detailed structural fragmentation of MG after degradation was explored by the liquid chromatography−mass chromatography (LC−MS) technique. Finally, the scavenging activity of Co_3O_4 NPs was determined using different scavengers to confirm the free-radical formation.

RESULTS AND DISCUSSION

Formation Mechanism. An octahedron-shaped Co_3O_4 NPs was fabricated via a sol−gel method, and its formation mechanism is presented in Scheme 1. $C_4H_5O_4Na$ was used as a chelating/structure-directing agent for the fabrication of Co_3O_4. In the initial stage, $C_4H_5O_4Na$ reacts with Co^{2+} ions in solution, forming a cobalt−succinate complex (Figure S1b). After addition of $NaC_{12}H_{25}SO_4$ as the surfactant, it attaches to the surface of the cobalt−succinate complex, and its morphology turns spherical [Figure S2]. Due to the presence of free oxygenated coordination sites in $C_4H_5O_4Na$, a lone pair of oxygen electrons coordinates with Co^{2+}, which is in agreement with the UV−visible spectra [Figure S1a,b].

The UV−visible spectrum shows the reduced peak intensity of free Co^{2+} ions after the addition of $C_4H_5O_4Na$, which signifies that interactions took place at the co-ordination site of

https://dx.doi.org/10.1021/acsomega.9b03998
ACS Omega 2020, 5, 7823−7835

$C_4H_5O_4Na$. Furthermore, the peak intensity remains unchanged after the addition of $NaC_{12}H_{25}SO_4$ (Figure S1c), authenticating the idea that $NaC_{12}H_{25}SO_4$ does not have strong interactions with Co^{2+}. Thus, as per the proposed mechanism, $NaC_{12}H_{25}SO_4$ assembles on the surface of the $C_4H_5O_4Na{-}Co^{2+}$ complex. The complex formation with $C_4H_5O_4Na$ at a certain temperature was responsible for the growth of Co_3O_4 crystals with selective facets. In addition, it was controlled by the addition of $NaC_{12}H_{25}SO_4$ that has inherent physicochemical properties. It adopts different morphologies such as micelles, vesicles, etc. through concentration variation. During the growth of the $C_4H_5O_4Na{-}Co^{2+}$complex into a crystal, $NaC_{12}H_{25}SO_4$ plays a crucial role in the formation of exclusive octahedron-shaped Co_3O_4. It deposits on the surface of octahedron Co_3O_4 through self-assembly via hydrophobic interactions among the long hydrocarbon chains. Co_3O_4 has a tendency to form a sphere (Figure S2), and $NaC_{12}H_{25}SO_4$ inhibits the alteration of octahedral phases to other morphologies.

Crystal Structure. The phase and crystal structure of the synthesized Co_3O_4 NPs were investigated by XRD, and the XRD pattern of precalcined Co_3O_4 shows weak diffraction peaks [Figure 1a]. However, the diffraction pattern of calcined

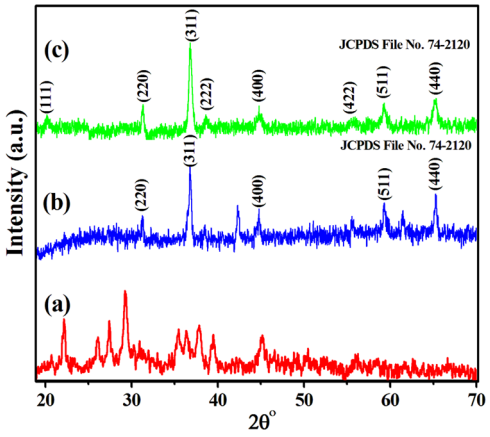

Figure 1. XRD patterns of (a) precalcined and (b) calcined without SDS and (c) calcined with SDS Co_3O_4 NPs.

Co_3O_4 NPs without SDS [Figure 1b] showed well-defined reflections at 31.30, 36.75, 44.94, 59.53, and 65.38° corresponding to the (220), (311), (400), (511), and (440) lattice planes compared to that of precalcined Co_3O_4. With SDS, Co_3O_4 NPs [Figure 1c] show the presence of well-defined peaks at 20.11, 31.08, 36.67, 38.57, 44.69, 55.76, 59.24, and 65.25° corresponding to the (111), (220), (311), (222), (400), (422), (511), and (440) lattice planes, indicating a more crystalline nature compared to that calcined without SDS and the precalcined Co_3O_4. The patterns were indexed to the face-centered cubic (FCC) spinel structure and well supported by JCPDS (74-2120). Additionally, no extra patterns were observed for the other phases of Co_xO_y, confirming the purity of the material. The lattice parameter of calcined Co_3O_4 was found to be 8.08 Å with the *Fd*-3*m* space group, and the average crystallite size of spinel-Co_3O_4 was estimated using Debye–Scherer's equation, which was in the range of 23–29 nm.[39,40] Moreover, the presence of only cobalt (Co) and oxygen (O) atoms in the EDS spectrum (Figure S3) confirmed the purity, which is well supported by the XRD study.

Thermal and Pore Size Analysis. The thermal stability of precalcined and calcined Co_3O_4 NPs was examined by TG [Figure 2a,b]. The detailed thermal degradation pathway of

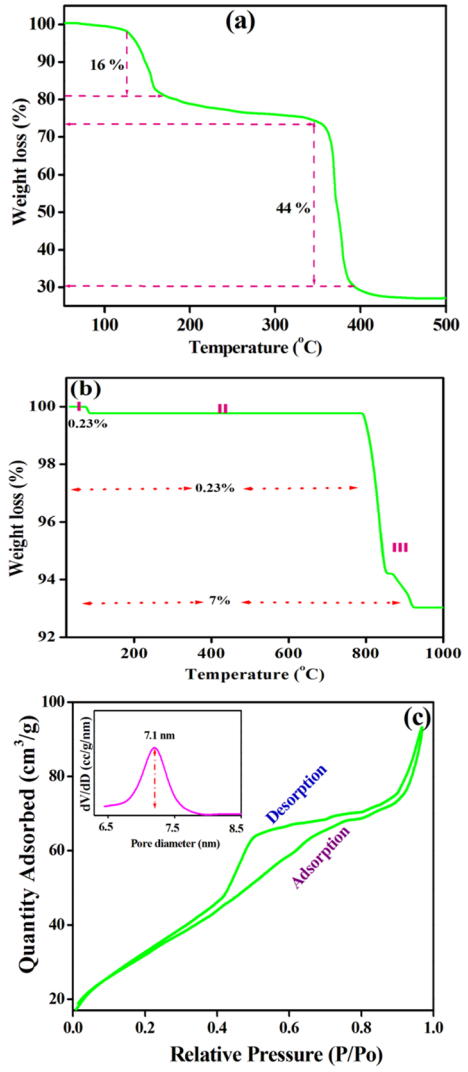

Figure 2. Thermograph of (a) precalcined and (b) calcined Co_3O_4 NPs and (c) N_2 adsorption–desorption isotherm of Co_3O_4 NPs.

calcined Co_3O_4 NPs is depicted in Scheme 2. However, a detailed discussion and the mechanism of precalcined Co_3O_4 NPs is presented in the Supplementary Information (Scheme S1). The thermograph of the calcined Co_3O_4 NPs showed a three-step thermal disintegration process. Initially, Co_3O_4 NPs showed that an insignificant weight loss (0.23%) took place between 48 and 120 °C, corresponding to the removal of the adsorbed water (Table S1). In the second step, no mass loss was observed at 120 °C, and this was retained up to 798 °C due to the chelate ring of the oxygen ions of succinate with the Co^{2+} moiety. Furthermore, a fraction of mass loss (7%) occurred between 798 and 902 °C in the third step of thermal degradation, attributed to the opening of the chelate ring (O_2), and eventually reaches a constant mass above 900 °C, due to the partial conversion of Co_3O_4 to a stable CoO state, forming ($3Co_3O_4 \rightarrow 6CoO{\cdot}Co_3O_4 + O_2$), i.e., the $CoO{\cdot}Co_3O_4$ adduct.[25] This is well supported by the XRD pattern (Figure S4, calcined at 900 °C for 5 h), which displayed the mixed phases of $CoO{\cdot}Co_3O_4$ (JCPDS no. 72-1474).[41] The half-

https://dx.doi.org/10.1021/acsomega.9b03998
ACS Omega 2020, 5, 7823–7835

Scheme 2. Thermal Degradation Mechanism of Calcined Co_3O_4 NPs

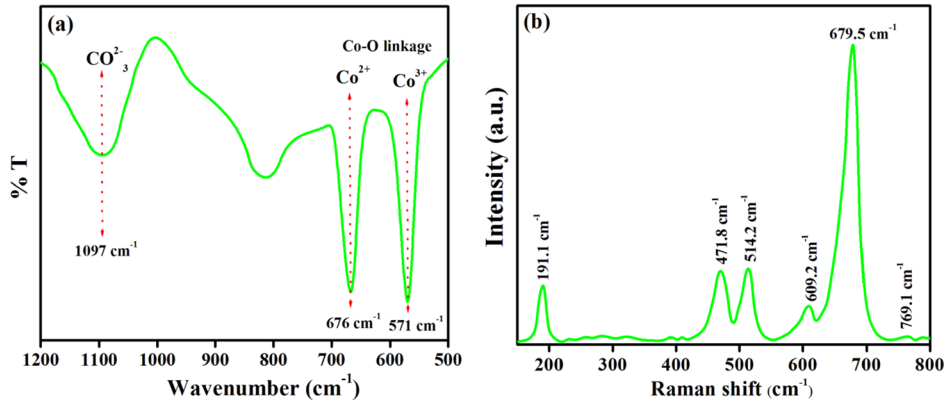

Figure 3. (a) FT-IR spectrum and (b) Raman spectrum of Co_3O_4 NPs.

decomposition temperature (HDT), temperature range, and degraded materials at each step are provided in Table S1. The corresponding reaction at 900 °C can be described as

$$3Co_3O_4 \rightarrow 6CoO{\cdot}Co_3O_4 + O_2$$

Our hypothesis sought for the structural changes during heat treatment based on the TG results; the precalcined material has a cobalt complex, i.e., [Co (II) $(C_4H_4O_4^{2-})_2{\cdot}(H_2O)_2$] $4H_2O$, while the calcined material has pure spinel-Co_3O_4. In conclusion, calcined Co_3O_4 has high thermal stability, and therefore, it was tested for the photocatalytic degradation of organic dyes. Therefore, the surface area, pore size distribution, and pore volume of the prepared material were investigated using the nitrogen (N_2) adsorption−desorption isotherm, and the adsorption isotherm [Figure 2c] is in agreement with the type IV isotherm with an H_3 hysteresis loop typical of an asymmetric, interconnected mesoporous structure. Moreover, the material exhibits a monodisperse pore size of ∼7.1 nm and a surface area of 69 m^2/g, which are generally favorable for adsorption and catalysis applications.

FT-IR and Raman Spectroscopy. The FT-IR spectrum of the Co_3O_4 NPs was recorded from 500 to 4000 cm^{-1}, and the results are shown in the supplementary information (Figure S5). As shown in Figure 3a, the broad IR band at 1097 cm^{-1} is assigned to the symmetric stretching of the CO_3^{2-} ion, and the two sharp peaks at 676 and 571 cm^{-1} are ascribed to the (Co−O) linkage fingerprint stretching vibrational modes that consequently confirm the formation of Co_3O_4 NPs.[42,43] In specific, the bands at 676 and 571 cm^{-1} are characteristic of Co−O bonding vibrations, signifying the occurrence of Co^{3+} ions and Co^{2+} ions at the octahedral and tetrahedral sites, respectively, of the spinel-Co_3O_4 crystal lattice.

Moreover, Raman shifts were used to analyze spinel-Co_3O_4 along with the *Fd*3*m* space group symmetry equation as follows:

$$\Gamma = A_{1g}(R) + E_g(R) + F_{1g}(IN) + 3F_{2g}(R) + 2A_{2u}(IN) + 2E_u(IN) + 4F_{1u}(IR) + 2F_{2u}(IN)$$

where R is the Raman active vibration, IR is the infrared-active vibration, and IN is the inactive mode.[28] The Raman spectrum shown in Figure 3b shows the presence of five prominent peaks at 191.1, 471.8, 514.2, 609.2, and 679.5 cm^{-1} corresponding to F^1_{2g}, E_g, F^2_{2g}, F^3_{2g}, and A_{1g}, respectively. Co_3O_4 has a normal spinel structure containing $Co^{2+}(Co^{3+})_2O_4^{2-}$, which was constituted by CoO_6 (octahedra) and CoO_4 (tetrahedra).[41] The A_{1g} mode contributes to the symmetric Co^{3+}−O stretching vibration. However, the bands at 471.8 and 514.2 cm^{-1} correspond to the E_g and F^2_{2g} symmetry, and F^1_{2g} and A_{1g} are attributed to the vibration of the Co_3O_4 tetrahedra. The nonexistence of any extra peaks again confirms the high purity of the synthesized Co_3O_4 NP. Furthermore, all the peaks were shifted toward higher wavelengths compared to the reported peak position[42] due to the size effects or the surface stress/strain.[42]

Morphological Exploration. The morphological characteristics of the Co_3O_4 NPs synthesized in the absence or presence of SDS were analyzed by SEM and TEM, as shown in Figure 4. The morphology of Co_3O_4 synthesized in the absence of SDS [Figure 4a,b] is consistent with spherical particles. On the other hand, a nearly uniform octahedron-shaped morphology was observed for Co_3O_4 NPs synthesized in the presence of SDS, as clearly shown in the HR-SEM images of Figure 4c,d.

Moreover, Figure 4d shows smooth surfaces and a well-defined octahedron shape with high-pitched corners and edges. The length of each edge of the octahedron Co_3O_4 NPs was about 50 to 75 nm.[29] The scaffold morphology is essentially derived from $C_4H_5O_4Na$, which plays a key role in the formation of uniform octahedron Co_3O_4 NPs because it acts as a chelating agent, where the free Co^{2+} ions occupy the octahedron coordination sites by oxygen atoms arising from two succinate ions and two hydroxyl groups producing a geometry of diaqua disuccinato Co(II) hydrate. Furthermore, this complex assembles into a near sphere along the edges (Figure S2), which was further calcined to obtain the final desired morphology. After slow addition of the SDS solution to the Co−succinate complex, the SDS molecules assemble through hydrophobic interactions between the long hydrophobic chains, leading to anchoring of the SDS chains on the surface of the Co−succinate complex. After several washes to remove the residual traces of organic materials, the desired

https://dx.doi.org/10.1021/acsomega.9b03998
ACS Omega 2020, 5, 7823−7835

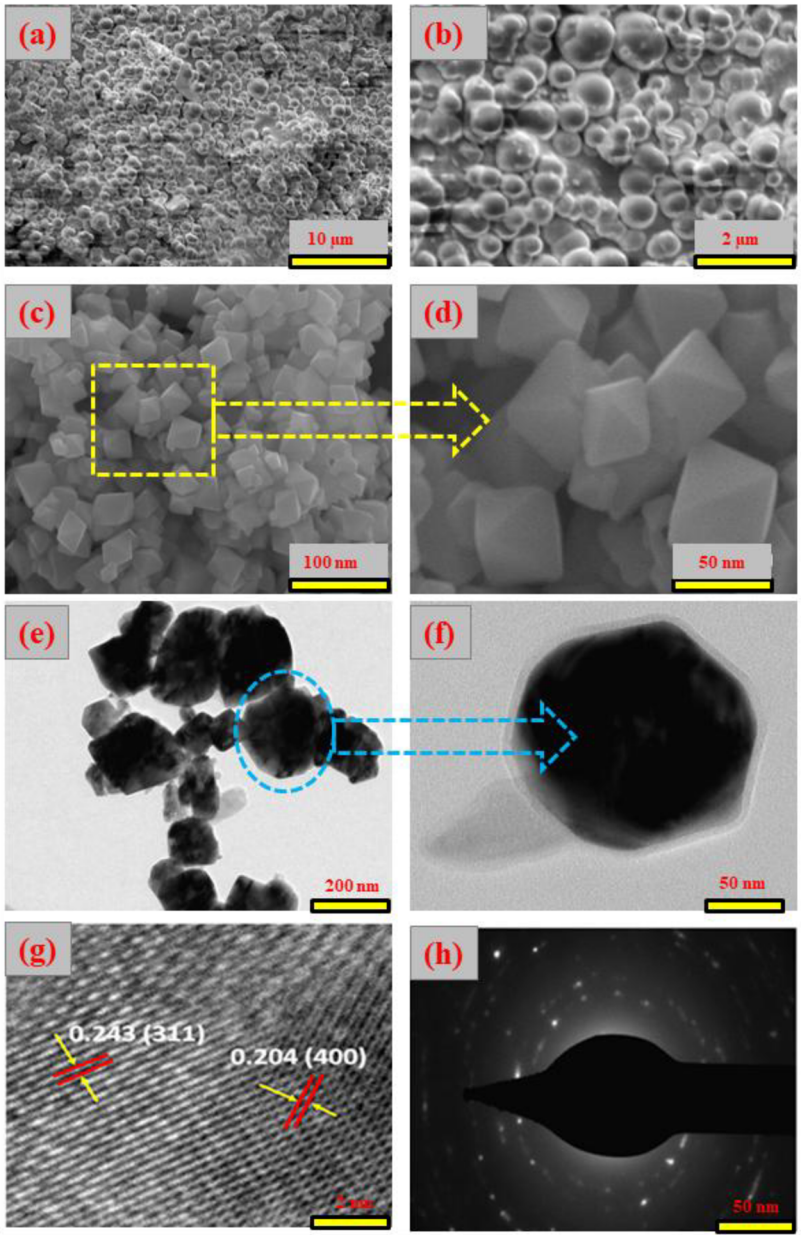

Figure 4. (a, b) SEM image of Co_3O_4 NPs, (c, d) without SDS, (e, f) TEM, (g) HR-TEM, and (h) SAED pattern of Co_3O_4 NPs with SDS.

morphology of uniformly distributed octahedron-shaped Co_3O_4 is obtained by calcination at 500 °C.[5,6,45,46] Furthermore, the TEM images of Co_3O_4 NPs [Figure 4e,f] clearly show the octahedron nature of the single Co_3O_4 NP having a core shell size of 3.2 nm and confined by the face normal projection of the octahedron [Figure 4e], with average sizes of 50−75 nm. Moreover, the measured d-spacing of 0.243 nm is attributed to the (311) plane and 0.204 nm to the (400) plane of Co_3O_4 NPs [Figure 4g], which are consistent with the XRD data.[47] Moreover, the selected area electron diffraction (SAED) pattern of Co_3O_4 NPs [Figure 4h] reveals a ring-like pattern, indicating the polycrystalline nature of Co_3O_4 NPs.

XPS Analysis and Bad Gap Energy. The XPS survey and high-resolution C1s, Co2p, and O1s spectra of spinel-Co_3O_4 are depicted in Figure 5. Four notable peaks at 284.7 eV (C1s), 529.9 eV (O1s), 779.7 eV (Co2p), and 794.4 eV (Co2p) were observed in the XPS survey spectrum [Figure 5a]. The peak at 284.7 eV in the C1s HR spectrum shown in Figure 5b is assigned to the adventitious C−C hydrocarbon bond, which is used for the calibration of the binding energy scale. The prominent peak of the Co2p3/2 level is deconvoluted into two peaks at 779.78 and 794.49 eV [Figure 5c], attributed to the $Co^{3+}2p_{3/2}$ (in octahedron site species) and Co^{2+} 2p3/2 (in tetrahedral sites species) conformation, respectively.[44] The exact oxidation state of Co can be induced from the spin−orbit splitting of the Co2p ($2p_{1/2}$) peak at 794.35−794.45 and 795.35−795.7 eV, assigned to Co^{3+}2p1/2 and Co^{2+}2p1/2 configurations, respectively.[43] Moreover, the shake-up peaks of the Co_3O_4 phase are also observed at 789 and 803.8 eV. The energy difference between Co2p3/2 and the main peak of Co2p1/2 is about 14.76 eV, which is characteristic of the Co_3O_4 (mixed Co(II)/Co(III) phase.[46−48] Consequently, the XPS analysis confirms the Co_3O_4 spinel structure. The O1s core level [Figure 5d] is related to the peak at 529.98 eV with a shoulder close to 531.1 eV corresponding to multiple oxygen species such as surface lattice oxygen, surface adsorbed oxygen,

https://dx.doi.org/10.1021/acsomega.9b03998
ACS Omega 2020, 5, 7823−7835

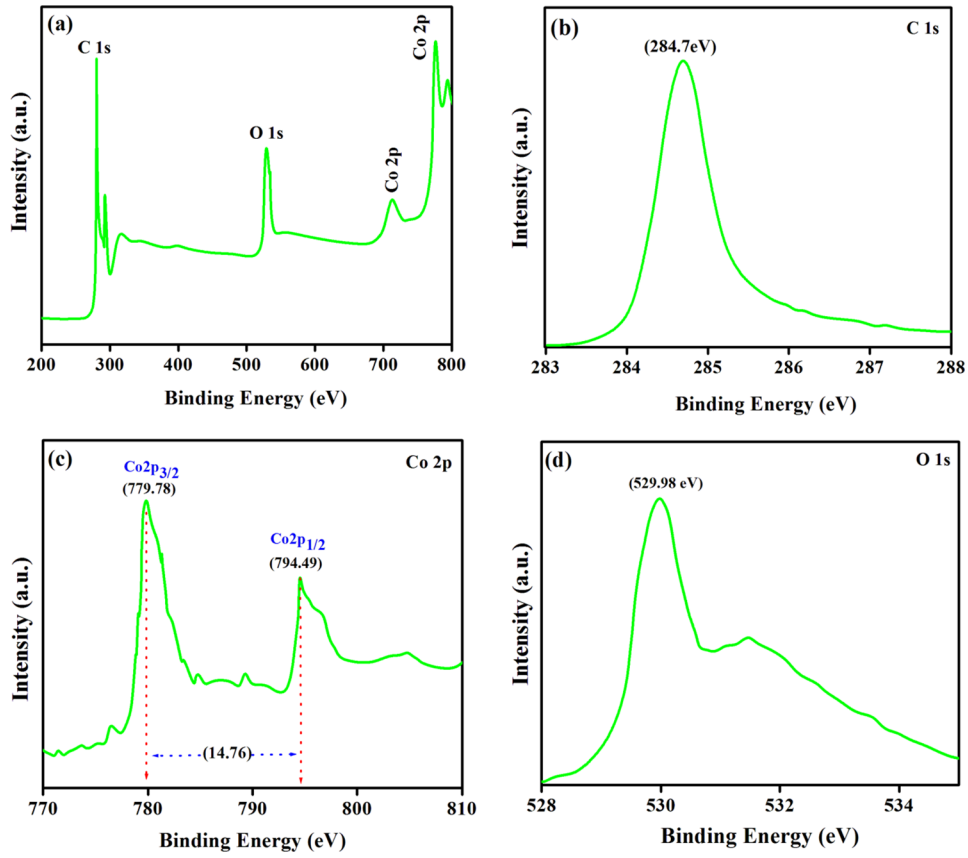

Figure 5. (a) XPS survey, (b) C1s, (c) Co2p, and (d) O1s spectra of Co_3O_4 NPs.

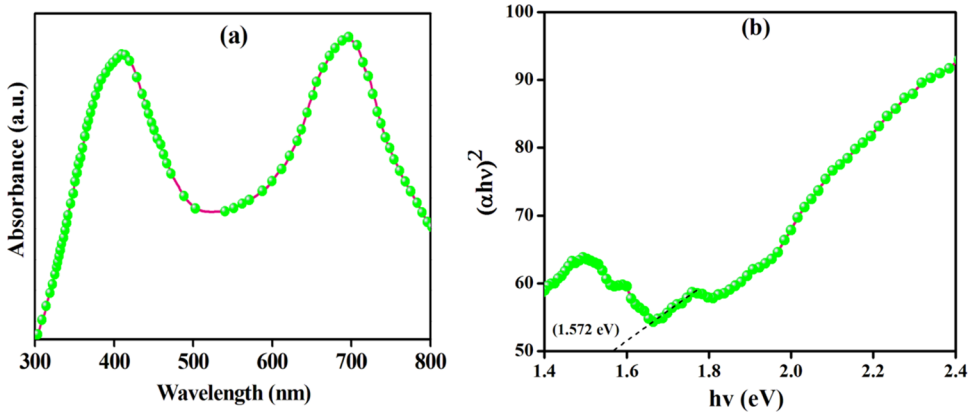

Figure 6. (a) UV-DRS spectrum and (b) $(\alpha h\nu)^2$ vs $h\nu$ for Co_3O_4 NPs.

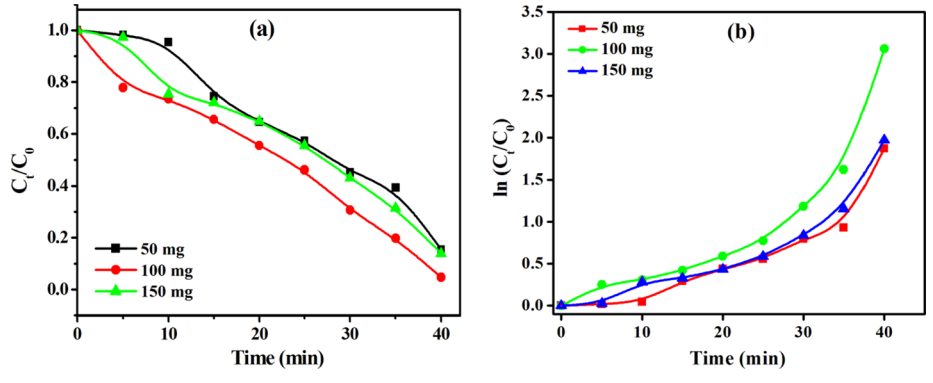

Figure 7. Effect of catalyst loading on (a) photodegradation and (b) $\ln(C_t/C_0)$ versus irradiation time.

https://dx.doi.org/10.1021/acsomega.9b03998
ACS Omega 2020, 5, 7823−7835

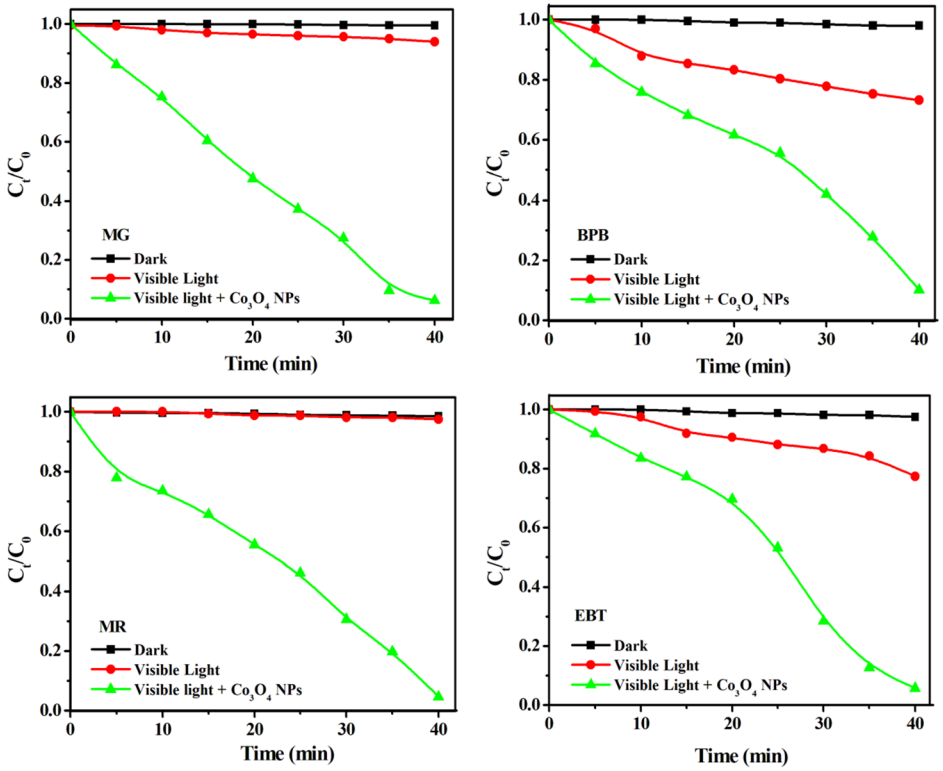

Figure 8. Co_3O_4-catalyzed time-dependent photodegradation of dyes under visible light.

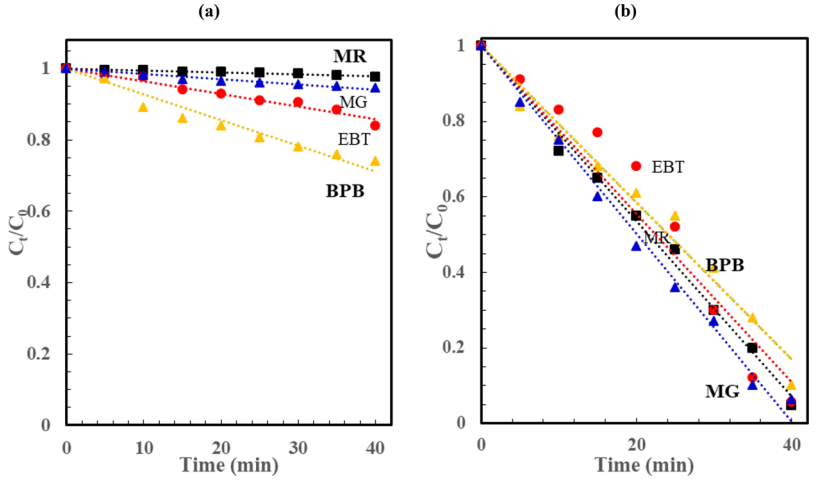

Figure 9. Normalized dye concentration versus visible light photodegradation time for various dyes in (a) the absence and (b) presence of the Co_3O_4 catalyst [dashed lines represent the linear fit of C_t/C_0 versus t].

and chemisorbed water in the Co_3O_4 crystal lattice attached to Co.[44]

The as-synthesized Co_3O_4 NPs have a p-type semiconducting nanostructure, and their diffuse reflectance spectroscopy (DRS) data [Figure 6a,b] reveal the presence of two absorption peaks at 408 and 694 nm due to the ligand−metal charge transfer (LMCT).[49] The Kubelka−Munk (K−M) model is used to estimate the optical band gaps of Co_3O_4 NPs:

$$\alpha h\nu = A(h\nu - E_g)^n$$

where α is the absorption coefficient, $h\nu$ is the photon energy, A is a constant, E_g is the band gap energy, and the exponent n is 2 for the direct band gap and **1/2** for the indirect band gap. Therefore, the band gap (E_g) for Co_3O_4 NPs was estimated from the linear fit of $(\alpha h\nu)^2$ versus $h\nu$, and it was found to be 1.572 eV [Figure 6b]. This band gap energy is attributed to the charge transfer of O^{II} to Co(II) and O^{II} to Co(III) and is expected to provide excellent photocatalytic activities.

Photocatalytic Performance. Visible light-induced photocatalytic degradation of MG, EBT, BPB, and MR was investigated using the mesoporous octahedron-shaped Co_3O_4 NPs. In order to study the influence of the catalyst dose on dye degradation efficiency, different doses (50, 100, and 150 mg) of Co_3O_4 NPs were used while keeping all other characteristics constant. Figure 7 shows the influence of catalyst dose on the degradation efficiency and reaction kinetics. A sharp decrease of the concentration of the corresponding dyes was observed [Figure7a], which was supported by the UV−visible spectra of

https://dx.doi.org/10.1021/acsomega.9b03998
ACS Omega 2020, 5, 7823−7835

Table 1. Percentage of Degradation, Rate Constant (k), and R^2 of Co_3O_4-Catalyzed Dye Degradation under Visible Light Irradiation[a]

		degradation at 40 min (%)		rate constant (k, mol m^{-3} h^{-1})		R^2	
dye	molecular formula	WC	PC	WC	PC	WC	PC
MR	$C_{15}H_{15}N_3O_2$	33.9	95.3	0.16	8.2	0.97	0.98
EBT	$C_{20}H_{12}N_3O_7SNa$	22.6	94.3	1.12	2.9	0.95	0.95
BPB	$C_{19}H_{10}Br_4O_5S$	26.7	89.8	0.39	2.8	0.94	0.97
MG	$C_{23}H_{25}ClN_2$	1.81	93.7	0.30	7.0	0.96	0.99

[a]WC: without catalyst; PC: presence of light and Co_3O_4 NPs.

dyes before and after treatment with Co_3O_4 NPs (Figure S7). Moreover, the reaction kinetics is pseudo-zero-order [Figure 7a] after 40 min of visible light irradiation. Initially at 50 mg, they show less degradation due to limited access to the catalyst surface and absorption of light. However, in 100 mg catalyst loading, significantly higher degradation was observed than in 50 and 150 mg loading owing to the availability of more effective active sites along with more interactions with dyes and the catalyst surface, which were more responsible for the enhanced deterioration of the corresponding dye.

The Co_3O_4-catalyzed photoactivity of dyes was monitored by the changes in the absorption spectrum of the dye solution as a function of time (Figure S8). As the irradiation time increases, the absorption peak height decreases for the corresponding dyes and reaches a flat pattern within 40 min of visible light irradiation, indicating degradation of more than 95% of the MR, EBT, BPB, and MG dyes. In addition, this was confirmed by the rapid change in the color of the dye solution (Figure S9). The rapid photocatalytic degradation of toxic dyes in the presence of Co_3O_4 NPs reflects the enhanced light harvesting, charge transfer, and separation. The time-dependent dye degradation under visible light irradiation is displayed in Figure 8. In contrast to very rapid degradation in the presence of Co_3O_4 NPs, it can be clearly seen that no degradation takes place in the dark or under visible light in the absence of Co_3O_4 NPs.

It is clearly seen that the patterns of the dye concentration profile of all dyes were almost identical and the dyes were fully degraded within 40 min in the presence of Co_3O_4 NPs, indicating the high catalyst activity for the degradation of the tested dyes.

As shown in Figure 8, there is near linear dependence of C_t/C_0 on irradiation time, which suggests that the process kinetics is pseudo-zero-order (rate = $-dC_t/dt = k$). Solving this equation leads to $C_t = C_0 - kt$ or $C_A/C_0 = 1 - (k/C_0)t$. Therefore, the slope of the linear fit of C_A/C_0 versus t is $-k/C_0$, where C_0 is the initial dye concentration (mol/m^3) ($C_0 = C_0$ (ppm)/M, M is the dye molecular weight) and k is the zero-order degradation rate constant (mol/m^3/min). Figure 9a,b shows the fitting of normalized dye concentration versus time for the various dyes under visible light illumination in the absence (Figure 9 a) and presence of Co_2O_3 NPs (Figure 9 b). Moreover, the reaction rate constant and the % dye degradation after 40 min are provided in Table 1. Among all the corresponding different dyes, MR shows enhanced photodegradation, and the photocatalytic degradation follows the order MR > EBT > MG > BPB. Furthermore, the degradation efficiency and reaction kinetics were thoroughly studied for MR, EBT, BPB, and MG dye degradation with Co_3O_4 NPs under visible light illumination [Figure 9b]. The Co_3O_4 NP-catalyzed rate constant follows pseudo-zero-order kinetics, and the pseudo-zero-order reaction constant is provided in Table 1. The present study shows more rapid Co_3O_4 NP-catalyzed photodegradation for all dyes including MG compared to previously reported Co_3O_4 and Co_3O_4–ZrO_2 nanocomposites.[50] Additionally, we examined the Co_3O_4 NP catalysis activity on the EBT-based effluent collected from industries, and the results are presented in Figure S10.

Catalyst Reusability. Recyclability of Co_3O_4 NPs was performed after complete deterioration of the corresponding dye; the NPs were recovered by filtration, washed multiple times, dried at 80 °C, and reused again. This was repeated for 4 cycles, and the result of the Co_3O_4 NP reusability in terms of % degradation in each cycle is presented in Figure 10. The results

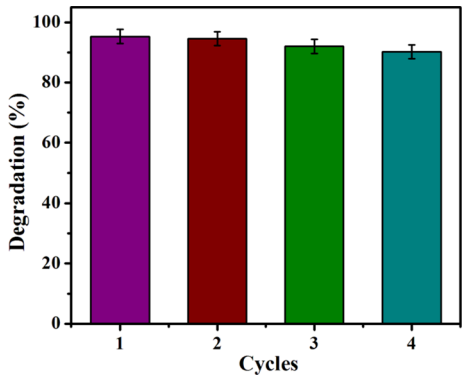

Figure 10. Reusability of Co_3O_4 NP-catalyzed dyes under visible light irradiation.

indicated no loss of photocatalytic efficiency up to the first 2 cycles, and a slight decrease in efficiency was observed during cycles 3 and 4. Moreover, the XRD pattern Figure S11) shows no changes in the structure and architectural stability of reusable Co_3O_4 NPs after 4 cycles compared to when calcined with Co_3O_4 NPs [Figure 1c].

Photodegradation Mechanism. A probable Co_3O_4 NP-catalyzed photodegradation mechanism under visible light irradiation is presented in Figure 11. The electrons (e^-) in the valence band were excited to a higher-energy conduction band along with the holes (h^+) of the corresponding Co_3O_4 NPs. The SDS-mediated Co_3O_4 NPs were treated under visible light, resulting in the migration of e^- from the valence band to the conduction band via a suitable band gap energy (E_g), which generates electron-deficient h^+. Due to this, the e^-–h^+ phenomenon occurs.[51−53] The e^-–h^+ pairs were present on the surface of the active Co_3O_4 catalyst, which was trapped by oxygen and water molecules, respectively, along with the corresponding dye molecules. Thus, surface-active Co_3O_4 permits the photogenerated charge carriers from the inside of the bulk to transfer to the surface to prevent the hole–electron recombination. Generally, the mesoporous nanostruc-

https://dx.doi.org/10.1021/acsomega.9b03998
ACS Omega 2020, 5, 7823−7835

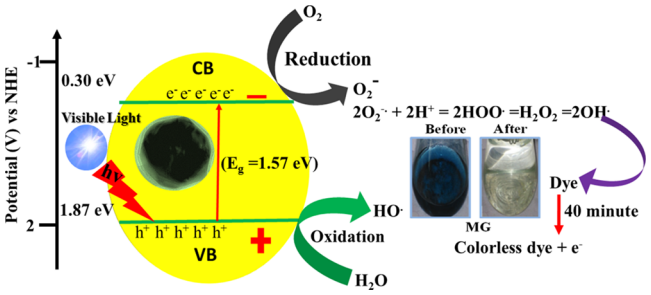

Figure 11. Possible mechanism of photoexcitation and dye decomposition using Co_3O_4 NPs.

ture, high surface area, and photoactive semiconductor catalysts facilitate faster electron relocation from the core to the surface of the corresponding catalyst.[51,52]

In the valence band portion, H_2O molecules were attached and converted themselves into active OH^- radicals via tricking H_2O molecules.[52] Concurrently, the electrons in the conduction band of the corresponding Co_3O_4 interacted with the dissolved molecular oxygen present in H_2O to produce a superoxide radical anion, which was further allowed to react with the H_2O molecule to produce ^-OH, which has powerful oxidizing ability. Due to the presence of such strong oxidizing agents, the corresponding dyes were oxidized and turned colorless.[12] It is highly notable that the morphology of metal oxide plays a key role in reducing the probability of electron–hole pair recombination, which is vital for efficient photocatalysis.[53−56] Photocatalytic semiconductor materials with 0D-, 1D-, 2D-, and 3D-like morphologies provide better photocatalytic activity compared to those with other disordered morphologies.[48,52] Apart from other effects of semiconductor materials, the band gap of the corresponding metal oxide is a key factor for enhanced photocatalytic activity. Therefore, in this manuscript, multiple parameters including mesoporosity, surface area, morphology, and tuned band gap energies collectively contribute to the enhanced visible light photocatalytic activity of octahedron-shaped Co_3O_4 NPs.

MG Degradation Study by LC–MS. The Co_3O_4 NP-catalyzed photodegradation products of MG after 5, 15, 25, 35, and 45 min of exposure to visible light were examined by LC–MS, and the mass spectra are presented in Figure 12. Before irradiation, i.e., at zero time, a sharp peak corresponding to MG at m/z = 364 was seen [Figure 12a]. After 5 min of exposure, the degraded MG residue shows a base peak at m/z = 329 [Figure 12b] due to loss of the chloride (Cl^-) ion. The other smaller peaks at m/z = 149, 181, and 212 are attributed to the split parts of MG ($C_6H_5COCHOCH_3^+$, $C_6H_5COC_6H_5^+$, and $C_6H_5COC_6H_4NH(CH_3)_2^+$, respectively). Visible light exposure to the MG dye solution [Figure 12c] for 15 min gave a base peak at m/z = 287, which arises due to the loss of three CH_2 molecules.

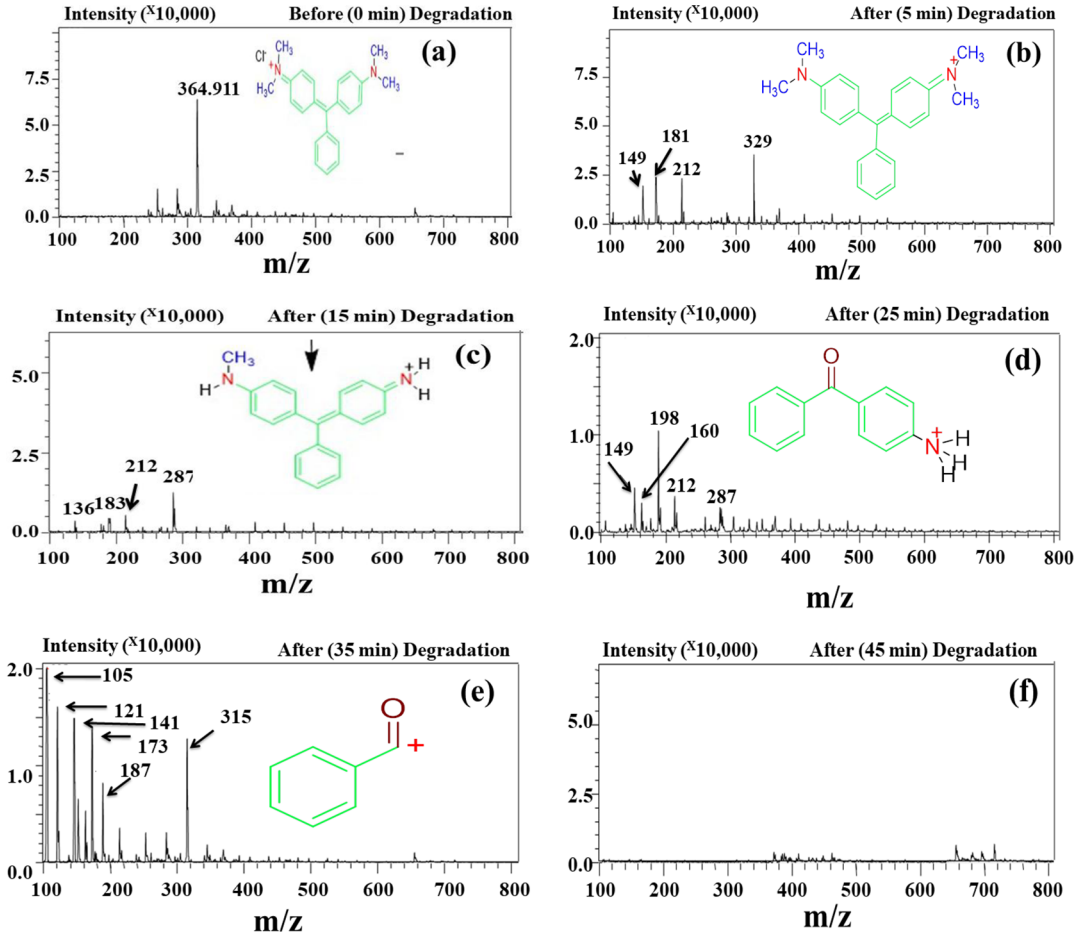

Figure 12. LC–MS spectra of the photodegradation products of MG at (a) 0 min (before degradation) and after (b) 5 min, (c) 15 min, (d) 25 min, (e) 35 min, and (f) 45 min.

https://dx.doi.org/10.1021/acsomega.9b03998
ACS Omega 2020, 5, 7823−7835

Moreover, the mass spectrum for the degradation products after 15 min shows peaks at m/z 136, 183, and 212, which correspond to $C_6H_5COCH_2NH_3^+$, $C_6H_5COHC_6H_5^+$, and $C_6H_5COC_6H_4NH(CH_3)_2^+$, respectively, in addition to the base peak at m/z 287 corresponding to tridesmethyl malachite green [Figure 12c], which is formed due to the N-demethylation of MG. After 25 min, the base peak was found to be at m/z 198, and the other peaks belong to $C_6H_5COCHO\ CH_3^+$, $C_{10}H_{10}NO^+$, $C_6H_5COC_6H_4NH(CH_3)_2^+$, and $NH_2C_6H_4CC_6H_5C_6H_4NHCH_3^+$ for m/z 149, 160, 212, and 287, respectively [Figure 12d]. At this stage, 62.74% of the dye was degraded. For complete dye degradation, irradiation was continued to 35 min [Figure 12e], and 90.45% of the MG dye was degraded; the product spectrum shows a base peak at m/z 105 due to the presence of benzyl ketone, and smaller peaks were observed at m/z 121, 141, 173, 187, and 315, which were attributed to $C_6H_5N(CH_3)_2^+$, $C_6H_5COHCl^+$, $C_6H_5CO(CH_2)_4NH_3^+$, $C_6H_5CO(CH_2)_5NH_3^+$, and $CH_3NCH_3C_6H_4CC_6H_5C_6H_4NHCH_3^+$, respectively (Scheme 3). The dye solution still contains some organic residue species

Scheme 3. Degradation Pathway of the MG Dye

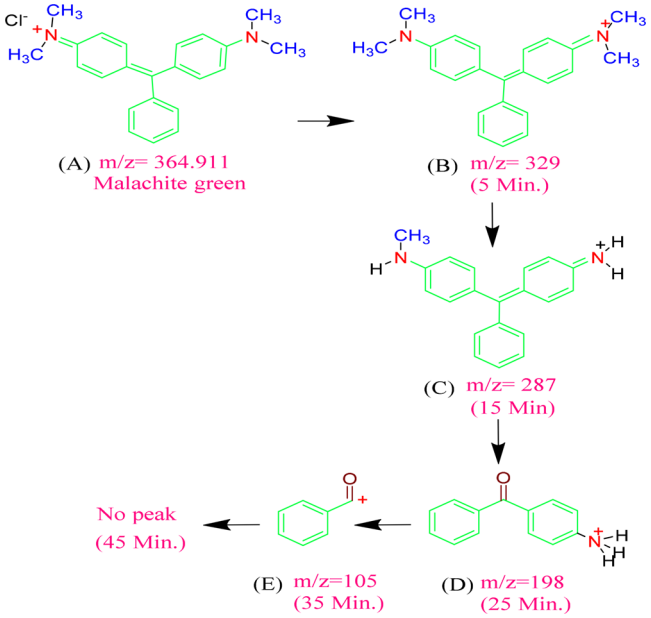

after 35 min of irradiation. Thus, the irradiation time was increased to 45 min and near 100% dye degradation was observed in the presence of Co_3O_4 NPs; the mass spectrum shows a small peak at m/z 400 due to the presence of some unknown impurities [Figure 12f]. The superior photocatalytic activity of the NPs was evidenced by comparing the near 100% degradation to the reported 42% MG degradation.[50] The photocatalytic degradation of the dye molecules is analyzed in terms of total organic carbon (TOC), and the results are depicted in [Figure S12].

Scavenging Effect. A scavenging study was carried out to confirm whether an active species was involved in the photocatalytic degradation of MG using KB, KI, ST, and BQ. The outcome of the MG assessment is presented in Figure 13 and Figure S13; their optical images are given in Figures S14 and S15. It has been well established that photogenerated holes (h^+), hydroxyl radicals ($^{\cdot}OH$), and superoxide species ($O_2^{\cdot-}$) plays a key role in the photodegradation process.[38] It

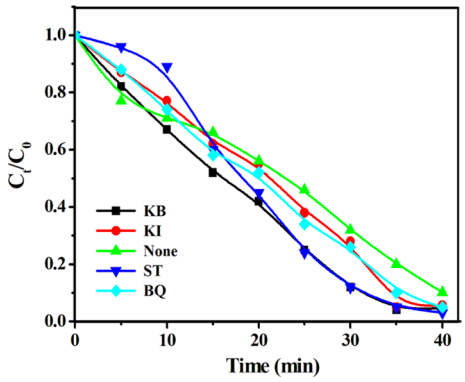

Figure 13. Scavenging test for the MG dye using KB, KI, ST, and BQ.

can be seen that, in different dyes, different scavenging materials played a role individually along with their photocatalytic pathway. However, KI played the key role of an excellent scavenger compared to its counterparts. The degradation of the four industrially toxic dyes was very significant when KI was used as the $O_2^{\cdot-}$ scavenger, which directly proved that the presence of $O_2^{\cdot-}$ species in the abovementioned photocatalytic reaction. The difference in the roles of the superoxide and $^{\cdot}OH$ radicals is very minute in their corresponding photocatalytic reaction [Figure 13 and Figure S13]. The photocatalytic patterns of the four dyes were entirely different when KB and ST were used as the scavenging agent. In the photocatalytic reaction mechanism, the photogenerated holes (h^+) were primarily the responsible species for the degradation of the aforementioned toxic dyes. Finally, the three species, hydroxyl ($^{\cdot}OH$), superoxide ($O_2^{\cdot-}$), and photogenerated holes (h^+), played important roles in the degradation of the corresponding dyes. The strong contribution of $^{\cdot}OH$, h^+, and $O_2^{\cdot-}$ in the reaction medium further supports the involvement of the photogenerated holes and electrons.[5]

CONCLUSIONS

The present work provides a simple synthetic method for tailoring the morphology, texture, and other physicochemical properties of Co_3O_4 NPs. Remarkably, SDS plays a key role in the formation of exclusively mesoporous, octahedron-shaped Co_3O_4 NPs with a narrow size distribution. Among spinel-type photocatalysts, the present mesoporous Co_3O_4 NPs show excellent photocatalytic performances under visible light irradiation toward degradation of MR, EBT, BPB, and MG dyes due to the presence of mesoporosity, scaffold morphology, surface area, and tuned band gap energy. The kinetics mechanism and radical confirmations were investigated using the scavenger assay. Moreover, the complete photochemical degradation of MG under visible light irradiation at different times was investigated by the LC−MS study.

EXPERIMENTAL SECTION

Materials and General Methods. Analytical-grade cobalt chloride hexahydrate ($CoCl_2{\cdot}6H_2O$), monosodium succinate ($C_4H_5O_4Na$), sodium dodecyl sulfate ($NaC_{12}H_{25}SO_4$), hydrazine hydrate (N_2H_4), methyl red (MR), Eriochrome Black-T (EBT), bromophenol blue (BPB), and malachite green (MG) as organic dyes; potassium iodide (KI), potassium bromate (KB), sodium thiosulfate (ST), benzoquinone (BQ) as

https://dx.doi.org/10.1021/acsomega.9b03998
ACS Omega 2020, 5, 7823−7835

scavengers; and ethanol and acetone as solvents were purchased from Merck, India, and used without further purification.

Fabrication of Co_3O_4 NPs. Co_3O_4 NPs were fabricated using a sol−gel method[35] (Scheme 1). In a typical procedure, 100 mL (0.1 M) of aqueous solution of $CoCl_2{\cdot}6H_2O$ was placed in a clean round-bottom flask and stirred at 50 °C for 15 min, and 50 mL of $C_4H_5O_4Na$ (0.26 M) was then added slowly into the hot solution and continuously stirred for another 20 min. Afterward, 10 mL of $NaC_{12}H_{25}SO_4$ (0.017 M) was added dropwise, and 1.5 mL of (5 M) N_2H_4 was added dropwise in order to hydrolyze and reduce the corresponding material. One hour after the addition of N_2H_4, a pinkish-white color gel appeared, and it was collected through centrifugation, washed with an ethanol/acetone mixture, dried at 60 °C in a preheated vacuum oven, and finally calcined at 500 °C for 3 h in a muffle furnace. The synthesized Co_3O_4 NPs were examined by various analytical techniques to determine their structural, compositional, and morphological features. The detailed characterizations of Co_3O_4 NPs are given in Supplementary Information S1.

Visible Light-Induced Photocatalytic Activity. The photocatalytic activity of the Co_3O_4 NPs was studied for the degradation of MR, EBT, BPB, and MG under visible light irradiation. The photocatalytic reactor was equipped with a cylindrical (400 W) tungsten lamp as a visible light source. Co_3O_4 NPs (100 mg) were dispersed in 100 mL of 20 ppm aqueous dye solution (pH = 6.5) at 25 ± 2 °C. Prior to light illumination, the suspension was stirred in the dark for 60 min for adsorption−desorption equilibrium. Afterwards the 100 mL suspension was exposed to visible light in the photocatalytic reactor. The solution (5 mL) was removed from the reactor at 5 min intervals and centrifuged to eradicate the corresponding photocatalyst; then, its absorption was measured using a UV−vis spectrophotometer (UV-1800, Shimadzu, Japan), and the dye degradation percentage was calculated from the concentration of the initial dye (20 ppm) (C_0) and the dye concentration at time t of the visible light exposure (C_t) as follows:

$$\text{degradation (\%)} = \{(C_0 - C_t)/C_0\} \times 100$$

The apparent zero-order rate constant (k, mol m^{-3} h^{-1}) of the degradation reaction catalyzed using the Co_3O_4 photocatalyst is determined by plotting C_t/C_0 versus irradiation time (t) using the following equation:

$$C_t = C_0 - kt$$

Detection of Trapping Species. For the holes and radicals, the trapping test was carried out by adding 0.1 mmol of scavengers (KI, KB, ST, and BQ) to the corresponding nanostructured octahedral Co_3O_4 NPs, and the holes (h^+), hydroxyl radicals ($^{\cdot}OH$), and superoxide radical anions ($O_2^{\cdot-}$) were detected in the corresponding photocatalytic dye degradation.

■ ASSOCIATED CONTENT

Supporting Information

The Supporting Information is available free of charge at https://pubs.acs.org/doi/10.1021/acsomega.9b03998.

Section S1: Characterization of Co_3O_4 NPs; Figure S1: different reaction steps and their corresponding UV−visible spectra; Figure S2: SEM images of before-calcined Co_3O_4 NPs; Figure S3: EDS spectrum of calcined Co_3O_4NPs; Figure S4: XRD profile of the mixed phase $CoO{\cdot}Co_3O_4$; Figure S5: FT-IR spectra; Figure S6: Mott−Schottky plot; Figure S7: UV−visible spectra; Figure S8: changes in UV−vis absorption pattern; Figure S9: photos of the corresponding dye degradation; Figure S10: photocatalytic degradation of the industrial effluent; Figure S11: XRD pattern of reused Co_3O_4; Figure S12: TOC removal after 240 min; Figure S13: scavenging test; Figure S14: photos of the corresponding dyes (MG and MR); Figure S15: photos of the scavenging test for EBT and BPB; Scheme S1: thermal degradation mechanism; and Table S1: thermal data (PDF)

■ AUTHOR INFORMATION

Corresponding Authors

Ratiram Gomaji Chaudhary − *Post Graduate Department of Chemistry, Seth Kesarimal Porwal College of Arts, Science and Commerce, Kamptee 441001, Maharashtra, India;* orcid.org/0000-0002-7874-585X; Email: chaudhary_rati@yahoo.com

Aniruddha Mondal − *Department of Chemical Engineering, Tatung University, Taipei 104, Taiwan;* Email: aniruddhacsmcri@gmail.com

Ahmed A. Abdala − *Chemical Engineering Program, Texas A&M University at Qatar, Doha, Qatar;* Email: ahmed.abdala@qatar.tamu.edu

Authors

Vaishali N. Sonkusare − *Post Graduate Teaching Department of Chemistry, Rashtrasant Tukdoji Maharaj Nagpur University, Nagpur 440033, Maharashtra, India*

Ganesh S. Bhusari − *Research and Development Division, Apple Chemie India Private Limited, Nagpur 441108, Maharashtra, India*

Ajay K. Potbhare − *Post Graduate Department of Chemistry, Seth Kesarimal Porwal College of Arts, Science and Commerce, Kamptee 441001, Maharashtra, India*

Raghvendra Kumar Mishra − *IMDEA Materials, 28906 Getafe, Madrid, Spain;* orcid.org/0000-0002-6341-7036

Harjeet D. Juneja − *Post Graduate Teaching Department of Chemistry, Rashtrasant Tukdoji Maharaj Nagpur University, Nagpur 440033, Maharashtra, India*

Complete contact information is available at: https://pubs.acs.org/10.1021/acsomega.9b03998

Author Contributions

This work was collaboratively done by all authors whose names are stated in the paper. The fabrication work was done by V.S., A.K.P., and R.G.C. The photocatalytic performances, diagrammatic scheme preparation, and writing work were executed by V.S., G.B., A.M., and R.M. In addition, the electronic result data interpretation was done by A.A.A., R.G.C., and H.D.J.

Funding

The research work was funded by SERB, Govt. of India (No-SB/EMEQ-366).

Notes

The authors declare no competing financial interest.

https://dx.doi.org/10.1021/acsomega.9b03998
ACS Omega 2020, 5, 7823−7835

■ ACKNOWLEDGMENTS

The authors would like to acknowledge SERB, India, for financial support.

■ REFERENCES

(1) Silambarasu, A.; Manikandan, A.; Balakrishnan, K. Room-temperature superparamagnetism and enhanced photocatalytic activity of magnetically reusable spinel $ZnFe_2O_4$nanocatalysts. *J. Supercond. Novel Magn.* **2017**, *30*, 2631−2640.

(2) Ravichandran, A. T.; Srinivas, J.; Karthick, R.; Manikandan, A.; Baykal, A. Facile combustion synthesis, structural, morphological, optical and antibacterial studies of Bi1− xAlxFeO3 (0.0≤ x≤ 0.15) nanoparticles. *Ceram. Int.* **2018**, *44*, 13247−13252.

(3) Asiri, S.; Sertkol, M.; Guner, S.; Gungunes, H.; Batoo, K.; Saleh, T. A.; Sozeri, H.; Almessiere, M. A.; Manikandan, A.; Baykal, A. Hydrothermal synthesis of $Co_yZn_yMn_{1-2y}Fe_2O_4$nanoferrites: magneto-optical investigation. *Ceram. Int.* **2018**, *44*, 5751−5759.

(4) Vadivel, S.; Saravanakumar, B.; Kumaravel, M.; Maruthamani, D.; Balasubramanian, N.; Manikandan, A.; Ramadoss, G.; Hariganesh, S. Facile solvothermal synthesis of BiOImicrosquares as a novel electrode material for supercapacitor applications. *Mater. Lett.* **2018**, *210*, 109−112.

(5) Pradhan, A. C.; Senthamizhan, A.; Uyar, T. Electrospun Mesoporous Composite CuO− Co_3O_4/N-TiO_2 Nanofibers as Efficient Visible Light Photocatalysts. *Chemistry Select* **2017**, *2*, 7031−7043.

(6) Pradhan, A. C.; Uyar, T. Morphological Control of Mesoporosity and Nanoparticles within Co_3O_4−CuO Electrospun Nanofibers: Quantum Confinement and Visible Light Photocatalysis Performance. *ACS Appl. Mater. Interfaces* **2017**, *9*, 35757−35774.

(7) Rajoriya, S.; Bargole, S.; George, S.; Saharan, V. K. Treatment of textile dyeing industry effluent using hydrodynamic cavitation in combination with advanced oxidation reagents. *J. Hazard.Mater.* **2018**, *344*, 1109−1115.

(8) Mani, S.; Bharagava, R. Exposure to crystal violet, its toxic, genotoxic and carcinogenic effects on environment and its degradation and detoxification for environmental safety. *Rev. Environ. Contam.T.* **2016**, *237*, 71−104.

(9) Kim, Y. G.; Jo, W.-K. Efficient decontamination of textile industry wastewater using a photochemically stable n−n type CdSe/Ag_3PO_4heterostructured nanohybrid containing metallic Ag as a mediator. *J. Hazard. Mater.* **2019**, *361*, 64−72.

(10) Plachtová, P.; Medříková, Z.; Zbořil, R.; Tuček, J.; Varma, R. S.; Maršálek, B. Iron and iron oxide nanoparticles synthesized with green tea extract: differences in ecotoxicological profile and ability to degrade malachite green. *ACS Sustainable Chem. Eng.* **2018**, *6*, 8679−8687.

(11) Wan, Y.; Chen, J.; Zhan, J.; Ma, Y. Facile synthesis of mesoporous $NiCo_2O_4$ fibers with enhanced photocatalytic performance for the degradation of methyl red under visible light irradiation. *J. Environ. Chem. Eng.* **2018**, *6*, 6079−6087.

(12) Rathnasamy, R.; Santhanam, M.; Alagan, V. Anchoring of ZnO nanoparticles on exfoliated MoS_2 nanosheets for enhanced photocatalytic decolorization of methyl red dye. *Mater. Sci. Semicond. Process.* **2018**, *85*, 59−67.

(13) Lee, R. B.; Lee, K. L.; Lai, C. W.; Pan, G.-T.; Yang, T. C. K.; Juan, J. C. The relationship between iron and Ilmenite for photocatalyst degradation. *Adv. Powder Technol.* **2018**, *29*, 1779−1786.

(14) Bishnoi, S.; Kumar, A.; Selvaraj, R. Facile synthesis of magnetic iron oxide nanoparticles using inedible *Cynometra ramiflora* fruit extract waste and their photocatalytic degradation of methylene blue dye. *Mater. Res. Bull.* **2018**, *97*, 121−127.

(15) Hou, X.; Wang, X.; Mi, W. Progress in Fe_3O_4-based multiferroic heterostructures. *J. Alloy Compd.* **2018**, *765*, 1127−1138.

(16) O'Neill, C.; Hawkes, F. R.; Hawkes, D. L.; Lourenço, N. D.; Pinheiro, H. M.; Delée, W. Colour in textile effluents−sources, measurement, discharge consents and simulation: a review. *J. Chem. Technol. Biot.* **1999**, *74*, 1009−1018.

(17) Hayyan, M.; Hashim, M. A.; AlNashef, I. M. Superoxide ion: generation and chemical implications. *Chem. Rev.* **2016**, *116*, 3029−3085.

(18) Lachheb, H.; Puzenat, E.; Houas, A.; Ksibi, M.; Elaloui, E.; Guillard, C.; Herrmann, J.-M. Photocatalytic degradation of various types of dyes (Alizarin S, Crocein Orange G, Methyl Red, Congo Red, Methylene Blue) in water by UV-irradiated titania. *Appl. Catal. B: Environ.* **2002**, *39*, 75−90.

(19) Meenatchi, B.; Sathiya Lakshmi, V.; Manikandan, A.; Renuga, V.; Sharmila, A.; Deve, K. R. N.; Jaganathan, S. K. Protic ionic liquid assisted synthesis and characterization of ferromagnetic cobalt oxide nanocatalyst. *J. Inorg. Organomet. Polym. Mater.* **2017**, *27*, 446−454.

(20) Maruthamani, D.; Vadivel, S.; Kumaravel, M.; Saravanakumar, B.; Paul, B.; Dhar, S. S.; Habibi-Yangjeh, A.; Manikandan, A.; Ramadoss, G. Fine cutting edge shaped Bi_2O_3 rods/reduced graphene oxide (RGO) composite for supercapacitor and visible-light photocatalytic applications. *J. Colloid Interf. Sci.* **2017**, *498*, 449−459.

(21) Mathubala, G.; Manikandan, A.; Arul Antony, S.; Ramar, P. Enhanced photocatalytic activity of spinel $Cu_xMn_{1-x}Fe_2O_4$nanocatalysts for the degradation of methylene blue dye and opto-magnetic properties. *Nanosci. Nanotechnol. Lett.* **2016**, *8*, 375−381.

(22) Bomila, R.; Srinivasan, S.; Gunasekaran, S.; Manikandan, A. Enhanced photocatalytic degradation of methylene blue dye, opto-magnetic and antibacterial behaviour of pure and La-doped ZnO nanoparticles. *J. Supercond. Novel Magn.* **2018**, *31*, 855−864.

(23) Chaudhary, R. G.; Bhusari, G. S.; Tiple, A. D.; Rai, A. R.; Somkuvar, S. R.; Potbhare, A. K.; Lambat, T. L.; Ingle, P. P.; Abdala, A. A. Metal/Metal Oxide Nanoparticles: Toxicity, Applications, and Future Prospects. *Curr. Pharm. Des.* **2019**, *25*, 4013−4029.

(24) Wang, X.; Tian, W.; Zhai, T.; Zhi, C.; Bando, Y.; Golberg, D. Cobalt (II, III) oxide hollow structures: fabrication, properties and applications. *J. Mater. Chem.* **2012**, *22*, 23310−23326.

(25) Manickam, M.; Ponnuswamy, V.; Sankar, C.; Suresh, R. Cobalt oxide thin films prepared by NSP technique: Impact of molar concentration on the structural, optical, morphological and electrical properties. *Optik.* **2016**, *127*, 5278−5284.

(26) Kaviyarasu, K.; Manikandan, E.; Kennedy, J.; Maaza, M. A comparative study on the morphological features of highly ordered MgO:AgO nanocube arrays prepared via a hydrothermal method. *RSC Adv.* **2015**, *5*, 82421−82428.

(27) Kennedy, J.; Murmu, P. P.; Leveneur, J.; Markwitz, A.; Futter, J. Controlling preferred orientation and electrical conductivity of zinc oxide thin films by post growth annealing treatment. *Appl. Surf. Sci.* **2016**, *367*, 52−58.

(28) Basith, N. M.; Vijaya, J. J.; Kennedy, L. J.; Bououdina, M.; Jenefar, S.; Kaviyarasan, V. Co-doped ZnO nanoparticles: structural, morphological, optical, magnetic and antibacterial studies. *J. Mater. Sci. Technol.* **2014**, *30*, 1108−1117.

(29) Liotta, L. F.; Wu, H.; Pantaleo, G.; Venezia, A. M. Co_3O_4 nanocrystals and Co_3O_4−MO_x binary oxides for CO, CH_4 and VOC oxidation at low temperatures: a review. *Catal. Sci. Technol.* **2013**, *3*, 3085−3102.

(30) Xu, J.; Cheng, J. The advances of Co_3O_4 as gas sensing materials: a review. *J. Alloy Compd.* **2016**, *686*, 753−768.

(31) Singh, H.; Sinha, A. K.; Singh, M. N.; Tiwari, P.; Phase, D. M.; Deb, S. K. Spectroscopic and structural studies of isochronally annealed cobalt oxide nanoparticles. *J. Phy. Chem. Solids.* **2014**, *75*, 397−402.

(32) Litter, M. Heterogeneous photocatalysis: transition metal ions in photocatalytic systems. *Appl. Catal. B-Environ.* **1999**, *23*, 89−114.

(33) Warang, T.; Patel, N.; Fernandes, R.; Bazzanella, N.; Miotello, A. Co_3O_4 nanoparticles assembled coatings synthesized by different techniques for photo-degradation of methylene blue dye. *Appl. Catal. B-Environ.* **2013**, *132*, 204−211.

(34) Raja, P.; Bensimon, M.; Klehm, U.; Albers, P.; Laub, D.; Kiwi-Minsker, L.; Renken, A.; Kiwi, J. Highly dispersed PTFE/Co_3O_4

https://dx.doi.org/10.1021/acsomega.9b03998
ACS Omega 2020, 5, 7823−7835

flexible films as photocatalyst showing fast kinetic performance for the discoloration of azo-dyes under solar irradiation. *J. Photochem. Photobiol., A* **2007**, *187*, 332−338.
(35) Dhas, C. R.; Venkatesh, R.; Jothivenkatachalam, K.; Nithya, A.; Benjamin, B. S.; Raj, A. M. E.; Jeyadheepan, K.; Sanjeeviraja, C. Visible light driven photocatalytic degradation of Rhodamine B and Direct Red using cobalt oxide nanoparticles. *Ceram. Int.* **2015**, *41*, 9301−9313.
(36) Potbhare, A. K.; Chaudhary, R. G.; Chouke, P. B.; Yerpude, S.; Mondal, A.; Sonkusare, V. N.; Rai, A. R.; Juneja, H. D. Phytosynthesis of nearly monodisperse CuO nanospheres using Phyllanthus reticulatus/Conyza bonariensis and its antioxidant/antibacterial assays. *Mater. Sci. Eng. C.* **2019**, *99*, 783−793.
(37) Chaudhary, R. G.; Sonkusare, V. N.; Bhusari, G. S.; Mondal, A.; Shaik, D. P. M. D.; Juneja, H. D. Microwave-mediated synthesis of spinel $CuAl_2O_4$ nanocomposites for enhanced electrochemical and catalytic performance. *Res. Chem. Intermed.* **2018**, *44*, 2039−2060.
(38) Sonkusare, V. N.; Chaudhary, R. G.; Bhusari, G. S.; Rai, A. R.; Juneja, H. D. Microwave-mediated synthesis, photocatalytic degradation and antibacterial activity of α-Bi_2O_3microflowers/novel γ-Bi_2O_3microspindles. *Nano-Struct. Nano-Objects.* **2018**, *13*, 121−131.
(39) Packiaraj, R.; Devendran, P.; Venkatesh, K.; Manikandan, A.; Nallamuthu, N. Electrochemical Investigations of Magnetic Co_3O_4 Nanoparticles as an Active Electrode for Supercapacitor Applications. *J. Supercond. Novel Magn.* **2019**, *32*, 2427−2436.
(40) Valan, M. F.; Manikandan, A.; Antony, S. A. A novel synthesis and characterization studies of magnetic Co_3O_4 nanoparticles. *J. Nanosci. Nanotechnol.* **2015**, *15*, 4580−4586.
(41) Greenwood, N.; Earnshaw, A. *Chemistry of the Elements*, 2nd Edition; Butterworth-Heinemann, 1997.
(42) Diallo, A.; Beye, A. C.; Doyle, T. B.; Park, E.; Maaza, M. Green synthesis of Co_3O_4 nanoparticles via Aspalathus linearis: physical properties. *Green Chem. Lett. Rev.* **2015**, *8*, 30−36.
(43) Mansournia, M.; Rakhshan, N. Amine ligand-based hydrothermal synthesis of Co_3O_4 nanoparticles, characterization and magnetic study. *J. Mol. Struct.* **2016**, *5*, 714−720.
(44) Li, Y.; Qiu, W.; Qin, F.; Fang, H.; Hadjiev, V. G.; Litvinov, D.; Bao, J. Identification of cobalt oxides with Raman scattering and Fourier transform infrared spectroscopy. *J. Phys. Chem. C* **2016**, *120*, 4511−4516.
(45) Hu, L.; Peng, Q.; Li, Y. Selective synthesis of Co_3O_4 nanocrystal with different shape and crystal plane effect on catalytic property for methane combustion. *J. Am. Chem. Soc.* **2008**, *130*, 16136−16137.
(46) Casas-Cabanas, M.; Binotto, G.; Larcher, D.; Lecup, A.; Giordani, V.; Tarascon, J.-M. Defect chemistry and catalytic activity of nanosized Co_3O_4. *Chem. Mater.* **2009**, *21*, 1939−1947.
(47) Zhu, Y.; Liu, X.; Jin, S.; Chen, H.; Lee, W.; Liu, M.; Chen, Y. Anionic defect engineering of transition metal oxides for oxygen reduction and evolution reactions. *J. Mater. Chem. A* **2019**, *7*, 5875−5897.
(48) Chen, X.; Tang, B.; Luo, J.; Wan, Y. Towards high-performance polysulfone membrane: The role of PSF-b-PEG copolymer additive. *Micropor. Mesopor. Mater.* **2017**, *241*, 355−365.
(49) Baker, L. R.; Jiang, C.-M.; Kelly, S. T.; Lucas, J. M.; Vura-Weis, J.; Gilles, M. K.; Alivisatos, A. P.; Leone, S. R. Charge carrier dynamics of photoexcited Co_3O_4 in methanol: extending high harmonic transient absorption spectroscopy to liquid environments. *Nano Lett.* **2014**, *14*, 5883−5890.
(50) Singh, S. A.; Vemparala, B.; Madras, G. Adsorption kinetics of dyes and their mixtures with Co_3O_4−ZrO_2 composites. *J. Environ. Chem. Eng.* **2015**, *3*, 2684−2696.
(51) Liu, J.; Wang, D.; Wang, M.; Kong, D.; Zhang, Y.; Chen, J.-F.; Dai, L. Uniform two-dimensional Co_3O_4 porous sheets: facile synthesis and enhanced photocatalytic performance. *Chem. Eng.Technol.* **2016**, *39*, 891−898.
(52) Nosaka, Y.; Nosaka, A. Generation and detection of reactive oxygen species in photocatalysis. *Chem. Rev.* **2017**, *117*, 11302−11336.
(53) Xu, J.; Huo, F.; Zhao, Y.; Liu, Y.; Yang, Q.; Cheng, Y.; Min, S.; Jin, Z.; Xiang, Z. In-situ La doped Co_3O_4 as highly efficient photocatalyst for solar hydrogen generation. *Int. J. Hydrogen Energ.* **2018**, *43*, 8674−8682.
(54) Manikandan, A.; Durka, M.; Seevakan, K.; Antony, S. A novel one-pot combustion synthesis and opto-magnetic properties of magnetically separable spinel MnxMg1−xFe2O4(0.0≤ x≤ 0.5) nanophotocatalysts. *J. Supercond. Novel Magn.* **2015**, *28*, 1405−1416.
(55) Manikandan, A.; Hema, E.; Durka, M.; Seevakan, K.; Alagesan, T.; Antony, S. Room temperature ferromagnetism of magnetically recyclable photocatalyst of Cu1−xMnxFe2O4-TiO2 (0.0≤ x≤ 0.5) nanocomposites. *J. Supercond. Novel Magn.* **2015**, *28*, 1783−1795.
(56) Mathubala, G.; Manikandan, A; Antony, S; Ramar, P. Photocatalytic degradation of methylene blue dye and magneto-optical studies of magnetically recyclable spinel $Ni_xMn_{1-x}Fe_2O_4$ (x= 0.0−1.0) nanoparticles. *J. Mol. Struct.* **2016**, *1113*, 79−87.

https://dx.doi.org/10.1021/acsomega.9b03998
ACS Omega 2020, 5, 7823−7835